Performance of Monolithic Two- and Three-Terminal Perovskite/Silicon Tandem Solar Cells Under Varying Illumination Conditions

Philipp Wagner,* Philipp Tockhorn, Sebastian Hall, Steve Albrecht, and Lars Korte*

Research on perovskite/silicon tandem solar cells is chiefly focused on devices in either two- or four-terminal configurations (2T and 4T, respectively). Straying from these commonly investigated approaches, an alternative monolithically integrated device architecture using three terminals (3T) by combining a semi-transparent perovskite top cell with a silicon heterojunction bottom cell featuring interdigitated rear contacts is presented. In the presence of a p/n recombination junction between subcells, a quasi-2T configuration is obtained where the additional terminal functions as a current regulator. Thus, in contrast to 2T tandems, current matching between subcells is not necessary. Therefore, these devices are more stable against spectral variations, especially their voltages at maximum power point, as surplus current can be either injected into or extracted from the additional terminal. This is tested both by simulations and for the first time experimentally. Interestingly, the highest power conversion efficiency is not achieved by current matching but by maximizing current generation in the top cell. An experimental realization of a 3T tandem with p/n recombination junction and a power conversion efficiency of 24.9% is presented, thus confirming the general viability of the concept.

1. Introduction

Combining two photovoltaic semiconductor absorbers with different bandgaps into tandem solar cells (TSCs) is a promising route to achieve power conversion efficiencies (PCEs) that surpass the detailed balance limit of single-junction solar cells.[1] In TSCs, the incident solar spectrum is exploited more efficiently

P. Wagner, P. Tockhorn, S. Hall, S. Albrecht, L. Korte
Department Perovskite Tandem Solar Cells
Helmholtz-Zentrum Berlin
12489 Berlin, Germany
E-mail: philipp.wagner@helmholtz-berlin.de; korte@helmholtz-berlin.de

S. Albrecht
Fakultät IV – Elektrotechnik und Informatik
Technical University Berlin
10587 Berlin, Germany

The ORCID identification number(s) for the author(s) of this article can be found under https://doi.org/10.1002/solr.202200954.

by reducing transmission losses (in the top cell) and thermalization losses (in the bottom cell).[2] A broad variety of absorber materials can be used for this purpose. With the quick and successful development of perovskite solar cells achieving high efficiencies of up to 25.7%,[3,4] perovskite/silicon TSCs have become a very attractive research field.[5] Combining perovskites with silicon, a mature solar cell technology, is particularly interesting as perovskite-based solar cells feature potentially cost-effective fabrication routes.[6] New highly efficient devices using this technology have been reported in short succession[7–9] with a certified record efficiency of 31.3%.[10]

When combining two semiconductors in a tandem device, two configurations are commonly investigated: 1) a monolithic architecture with a front and a rear electrode and a recombination junction between subcells (two-terminal TSCs, 2T TSCs) and 2) an architecture where both subcells feature their individual electron and hole contacts and are mechanically stacked together (four-terminal TSCs, 4T TSCs).[11] For optimal operation of 2T TSCs, current matching is required as both subcells are connected in series, and the overall current is limited by the subcell providing a lower current.[12] This performance loss is, however, partially mitigated by a gain in fill factor (FF) when the device is not under current matching conditions.[12] For 4T TSCs, no such requirement needs to be met because here both subcells are electrically decoupled. This advantage, however, might be offset by an increased complexity in device fabrication and module integration.[13,14] As an alternative to these common approaches, a third option where three electrodes (two for holes and one shared for electrons; or vice versa) are employed[15] has recently gained interest.[16–33] These three terminal TSCs (3T TSCs) are monolithic devices that do not require current matching, and thereby combine the advantages of 2T and 4T TSCs.[16,18,25,26,34]

3T TSCs were introduced in 1980 as solar spectrum dividing devices based on III/V semiconductors,[15] which is still the dominating top cell material for these devices today.[16,19,21,26–32] This initial design featured an interdigitated front contact, a recombination layer between subcells, and a full-area electrode on its rear side. An alternative design has later been proposed by using a bottom cell with interdigitated back contacts (IBC) and a top cell with a single front contact.[25] A third option for realizing a

three-terminal device is employing a middle contact as the third electrode, which has been demonstrated *i.a.* in Ref. [17,33] as a means to individually characterize the subcells of a monolithic tandem device. Using a middle contact, which is usually realized as a rather thick transparent conductive oxide (TCO) layer, entails parasitic absorption losses in that layer and is potentially challenging for upscaling where high lateral conductivities are required to minimize electrical losses. If on the other hand an IBC bottom cell is adopted, these losses can be mitigated with the downside of a more complex bottom cell fabrication. Concerning perovskite-on-silicon-based 3T TSCs, there are several theoretical studies concerning optical and electrical properties[22–24] or annual energy yield,[20,31] but few experimental realizations have been presented in literature so far.[17,18,33,35] In the following, the abbreviation "3T TSCs" explicitly refers to a combination of perovskite and silicon as subcell absorbers if not stated otherwise.

In a simulation study, a potential advantage in annual energy yield was found for 3T TSCs over 2T and 4T TSCs for a vast variety of perovskite bandgaps, perovskite thicknesses, and climatic conditions[20] mainly due to a higher robustness against spectral variations. Similar results were reported in Ref. [31] for voltage-matched 3T modules. A record 3T TSC with a PCE of 29% (certified at 29.56% in 2T configuration) has recently been presented, thereby demonstrating that high efficiencies in the realms of state-of-the-art 2T and 4T TSCs can also be achieved experimentally.[35] Other studies have further shown that module integration of 3T TSCs can be realized by a combination of series and parallel subcell interconnection, thereby creating strings that require only one inverter (as in 2T TSCs).[36,37] In this series/parallel string integration for 3T TSCs, long strings can be used to mitigate inevitable end-of-string losses.[37,38] Such flexible interconnection further allows for the creation of voltage-matched strings where $m \times V_{top} = n \times V_{bottom}$, with m and n being the amount of top or bottom cells connected in series, and V_{top} and V_{bottom} the voltage at maximum-power point (MPP) of individual top and bottom cells, respectively.[38] Due to the logarithmic dependence of voltage on illumination intensity, a voltage-coupled tandem device is more robust against spectral variation than a current-matched one (i.e., a 2T TSC).[26] For further details on string interconnection of 3T TSCs, we refer to the cited literature and references therein as this is outside the scope of this article.

While 2T and 4T TSCs behave electrically in a relatively well-understood manner, the performance of 3T tandems depends on a couple of aspects such as which contact is shared, the bottom cell's doping type and configuration (middle contact[17] or interdigitated back contacts[18]), and whether a recombination junction (p/n or n/p) or a same polarity/antiparallel junction (p/p or n/n) is formed between subcells. In fact, there are twelve distinct "subtypes" of the 3T configuration, and it is important to state what specific kind of device is investigated.[19] The same 3T TSC can be operated using either of its three electrodes as the common contact (i.e., the contact that is shared by both subcells). These different contacting schemes are referred to as "loading topologies".[19] It has been shown in theory[19] and experimentally[34] for 3T TSCs based on III/V semiconductors on silicon that the maximum PCE of the same 3T TSC is identical regardless of what loading topology is used. Only the voltages change that must be applied to the three terminals in order to operate the
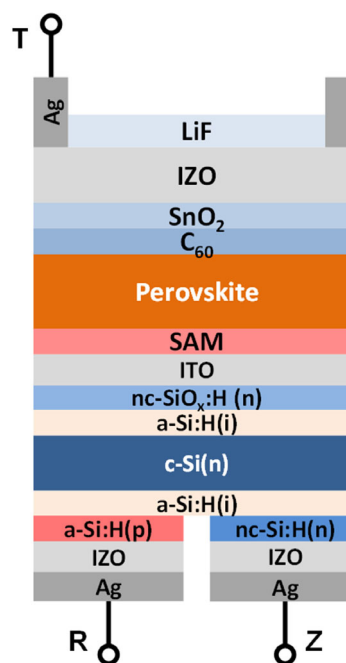

Figure 1. Schematic (not to scale) of a 3T perovskite/silicon heterojunction tandem solar cell with interdigitated rear contacts and a p/n recombination junction between subcells as investigated in this article. Details on each individual layer are given in the "experimental section." A textured rear side is present in the actual devices but is omitted here for clarity.

device at its global MPP and thus obtain its maximum efficiency. Depending on the exact subtype, 3T TSCs can show similar behavior to either their 2T or 4T counterparts. We find that the type of subcell interconnection (antiparallel or recombination junction) seems to be the key feature that defines different electrical behaviors in IBC 3T TSCs. In a previous publication, we have reported on an IBC 3T TSC with antiparallel n/n junction and a PCE of 17.1%.[18] Improvements to this original design have recently led to an increase in efficiency to 22.9%. Further details on the optimizations leading to this performance improvement in 3T TSCs with antiparallel junction can be found in the Supporting Information.

In this work, we investigate a different "subtype" of 3T TSC: we assess the influence of a p/n recombination junction on the overall performance of IBC 3T tandems (**Figure 1**a,b) and compare it to that of a 2T TSC with similar layer stack. An electrical model is developed to describe their electrical behavior, and the robustness of these devices against spectral variation is tested in simulation and experiment. Additionally, the influence of pinholes in the perovskite top cell is modeled by applying a low shunt resistance to the same electrical model.

2. Results and Discussion

2.1. Three-Terminal Perovskite/Silicon Tandem Solar Cells with P/N Recombination Junction

In this tandem design (Figure 1), a subcell interlayer stack similar to 2T TSCs is implemented. In fact, the device design

2200954 (2 of 10)

is almost exactly the same as in Ref. [7] only with an additional electron contact at the bottom cell's rear side and a different SAM as HTL. The interconnection scheme comprises a layer stack of nc-SiO$_x$:H(n) and ITO that forms a p/n recombination junction with the perovskite's HTL. This characteristic has a huge impact on the operation of this type of 3T TSC, and its electrical behavior differs drastically from that of devices with antiparallel junction (see Supporting Information and Ref. [18]). When contacting only electrodes R and Z on the rear of the device, the IBC bottom cell's j–V characteristics under illumination, filtered by the perovskite top cell's layers, are obtained (red curve in **Figure 2**). In case of using only electrodes T and R (i.e., the IBC bottom cell is being held at open-circuit conditions), the device can be operated as a regular 2T TSC (with reduced electrode area at its rear side) where voltages of both subcells add up and external current is limited by the lower one of each subcell's individual photocurrent (green curve in Figure 2). This measurement in "quasi-2T configuration" is in good agreement with numerically summing the j–V characteristics of both subcells (black curve in Figure 2), which is therefore a good estimate for the resulting tandem performance. 3T TSC in this configuration are thus a very versatile tool to investigate both subcells of a monolithic tandem device.

The maximum PCE of this 3T configuration is obtained if all three electrodes are contacted: applying bias voltages (in our case 0–640 mV) to terminals R and Z on the cell's rear shifts the $j_{T,R}$–$V_{T,R}$ characteristics to higher voltages because $V_{T,R}$ and $V_{R,Z}$ add up (**Figure 3**a). This behavior is similar to voltages of individual subcells adding up in a 2T TSC, and this part of the device is therefore denoted the "2T" subcircuit in the following. For $V_{R,Z} = 0$ V, which corresponds to the bottom cell being held under short-circuit conditions, the top cell's equivalent j–V characteristics, partly affected by resistive losses of the bottom cell, can be obtained (dashed black line in Figure 3a). This specific type of 3T TSC can therefore also be used as a measurement
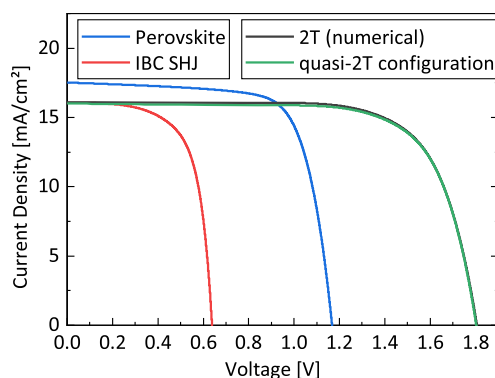
platform for 2T TSCs with identical layer stack, as also reported by others.[17,33] As a consequence of $V_{T,R}$ and $V_{R,Z}$ summing up, PCE$_{T,R}$ continuously increases for higher $V_{R,Z}$. The IBC bottom cell's power output (and thereby PCE$_{R,Z}$), however, becomes negative for all $V_{T,R}$ once the condition $V_{R,Z} > V_{oc,IBC}$ is met—in our case at ≈640 mV—because at this point more current is drawn from that subcell than it can provide. This limits the overall device performance, and therefore, the combined contribution of both subcircuits to the overall 3T TSC's power output needs to be considered. Displaying $j_{R,Z}$ (bottom cell current density) over $V_{T,R}$ (voltage across the "2T" subcircuit) provides information about injection/extraction of additional charge carriers into/from the IBC bottom cell (Figure 3b). This IBC subcircuit ($j_{R,Z}$–$V_{R,Z}$ for a given $V_{T,R}$) can be understood as a current regulator that counterbalances photocurrent mismatch between subcells: if the bottom cell features lower photogeneration than the top cell, additional current is injected into electrode Z to achieve current matching in the "2T" subcircuit, while for lower photogeneration in the top cell, additional current generated in the bottom cell can be extracted as additional power. If the device is already in a current-matched state and both subcells have sufficiently high shunt resistances, the additional electrode Z remains largely idle, and the tandem behaves as a regular 2T TSC. Since external current (at a given OP) can be injected into either subcell, a 3T TSC with p/n recombination junction can be biased toward a global MPP rather than one additionally constrained by current matching as in a 2T TSC. The full j–V characteristics of the "2T" and IBC subcircuit are given by performance maps displaying PCE$_{T,R}$ and PCE$_{R,Z}$ in a 2D contour plot versus $V_{T,R}$ and $V_{R,Z}$ (Figure 3c,d). The summation of both subcircuit performance maps yields the overall 3T TSC's PCE$_{3T}$ (Figure 3e). The combined contribution of both subcells at a variety of different bias voltages ($V_{T,R}$ and $V_{R,Z}$) leads to an overall maximum PCE$_{3T}$ of 24.9% (Figure 3e, white star) for our cell. This OP is achieved for $V_{T,R} = 1.44$ V and $V_{R,Z} = 0.52$ V, which are roughly $V_{T,R} = V_{MPP,perovskite} + V_{MPP,IBC}$ and $V_{R,Z} = V_{MPP,IBC}$. In other words, this device's voltage at MPP (particularly, $V_{T,R}$) is almost identical to that of a corresponding 2T TSC, which would feature a PCE$_{2T}$ of 24.8% (Figure 3e, blue star and dashed line) assuming $V_{MPP,2T} = V_{T,R,MPP}$.

The discussion here considers 3T TSC operation in so-called "common R mode" (i.e., the shared or common terminal is electrode R, the only hole contact of the device). It is, however, also possible to use electrode Z as shared contact ("common Z mode").[19,34] In this case, the device behaves similar to 3T TSCs with antiparallel junction that feature largely independent subcells as described in the Supporting Information and Ref. [18].

Figure 2. Measured current density–voltage characteristics of a 3T TSC with p/n recombination junction. For the perovskite top cell (blue), all three contacts are employed with $j_{T,R}$–$V_{T,R}$ being scanned with the IBC held at short-circuit conditions ($V_{R,Z} = 0$ V). For the IBC SHJ bottom cell (red), only terminals R and Z are used, whereas the front terminal T is kept floating. The black curve is a numerical summation of both subcell j–V characteristics, while the green curve is measured in "quasi-2T configuration" by using only terminals T and R. Corresponding solar cell parameters can be found in the Supporting Information.

2.2. Robustness Against Spectral Variation

To demonstrate the advantages of 3T over 2T TSCs under varying spectral conditions, we change photogeneration in the IBC bottom cell by increasing (or decreasing) the spectral irradiance of our LED solar simulator in the wavelength range between 800 and 900 nm (**Figure 4**a). These measurements are conducted for the device described in the previous section. We note that for the investigated device, the photogenerated current under

AM1.5g conditions is higher in the top cell than in the bottom cell. In Figure 4b–f, the current injected into or extracted through the additional terminal Z at different bias conditions is plotted against $V_{T,R}$ and $V_{R,Z}$ to visualize its function as a current regulator. The resulting current maps are superimposed with current density isolines and MPPs (black star symbols). For better clarity, only voltages around MPP are shown. Here, red (blue) colored portions represent current being extracted through (injected into) the bottom cell's additional terminal Z. Interestingly, the bias voltages ($V_{T,R}$ and $V_{R,Z}$) at which a maximum PCE_{3T} is achieved do not change appreciably with varying repartition of the photogenerated current between subcells (i.e., changing spectral conditions), which has important implications for developing an MPP tracking algorithm. Note that for strong changes in illumination intensity, there will also be a shift in these voltages. However, within the spectral variation in this experiment that results in a difference of up to 3.4 mA cm^{-2} in current injection/extraction from the bottom cell for the two extreme spectra (gray and green in Figure 4a), $V_{T,R}$ and $V_{R,Z}$ at MPP remain very stable despite a change in overall illumination intensity. In case of a higher photogenerated bottom cell current (Figure 4f), this

additional current in the IBC subcircuit is *extracted* through electrode Z for all operation points in the voltage range between $V_{T,R} = V_{MPP,perovskite} + V_{MPP,IBC}$ and $V_{R,Z} = V_{MPP,IBC}$ as indicated by the light-red shaded area. For $V_{R,Z} > V_{MPP,IBC}$ and $V_{T,R} < V_{MPP,perovskite} + V_{MPP,IBC}$, current is always injected into terminal Z because the IBC bottom cell cannot provide sufficient current anymore. This corresponds to a rapid decline in current generation between V_{MPP} and V_{oc} in the bottom cell's j–V characteristics. The same is true for the "2T" subcircuit if $V_{T,R}$ is applied outside the above defined voltage regime. This can be seen from the dark red flank in Figure 4b–f where the conditions $V_{T,R} = V_{oc,perovskite} + V_{R,Z}$ are met. These effects can also be seen from all performance maps presented throughout this article (both simulated and measured) and are not specific to the chosen device. In contrast, if the top cell's photogenerated current is higher, this surplus current is *injected* into terminal Z (light-blue-shaded area in Figure 4b–d). In case of equal photogeneration in both subcells (Figure 4e), which is equivalent to a current-matched 2T TSC, the additional terminal Z remains mostly idle for all OPs (i.e., set bias voltages) with a combination of bias voltages following the dashed isoline (white color).
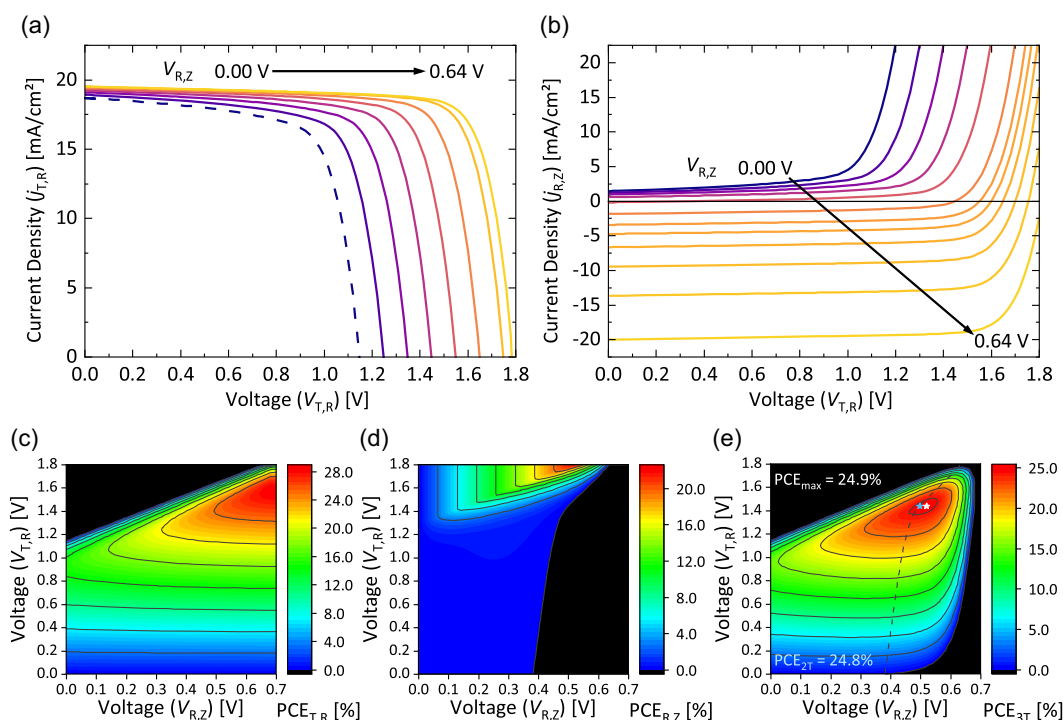

Figure 3. a) Measured current density–voltage characteristics of the "2T" subcircuit ($j_{T,R}$–$V_{T,R}$) of the best 3T TSC with p/n recombination junction as sketched in Figure 1 for different bias voltages $V_{R,Z}$ applied to the IBC subcircuit. The dashed curve at $V_{R,Z} = 0$ V is the top cell's single-junction j–V characteristics, modified by additional series resistance in the bottom cell. Voltages applied to both subcircuits ($V_{T,R}$ and $V_{R,Z}$) add up as in a 2T TSC. b) Current density–voltage characteristics of the IBC subcircuit as a function of $V_{T,R}$. Here, the current density ($j_{R,Z}$) that is injected into (negative sign) or extracted through (positive sign) the IBC bottom cell is measured. Every curve represents a constant $V_{R,Z}$ while $V_{T,R}$ is swept. c) Performance map showing the PCE of the "2T" subcircuit as a function of $V_{T,R}$ and $V_{R,Z}$. d) Same as (c) but for the PCE of the IBC subcircuit. e) Performance map of the best 3T TSC with p/n recombination junction calculated as the sum of (c) and (d). A maximum PCE_{3T} of 24.9% is achieved. The MPP is marked with a white star. The dashed isoline represents OPs where $j_{R,Z} = 0$ mA cm^{-2}, which corresponds to a quasi-2T configuration similar to that depicted in Figure 2. At these OPs, no current is extracted through the additional terminal Z and the 3T device behaves like a 2T TSC with its MPP (marked with a blue star) on the dashed line and a maximum PCE_{2T} of 24.8% (assuming $V_{MPP,2T} = V_{T,R,MPP}$). Note that the color scale in (c–e) is cut off at 0%. Also note that this is a different device than the one in Figure 2.
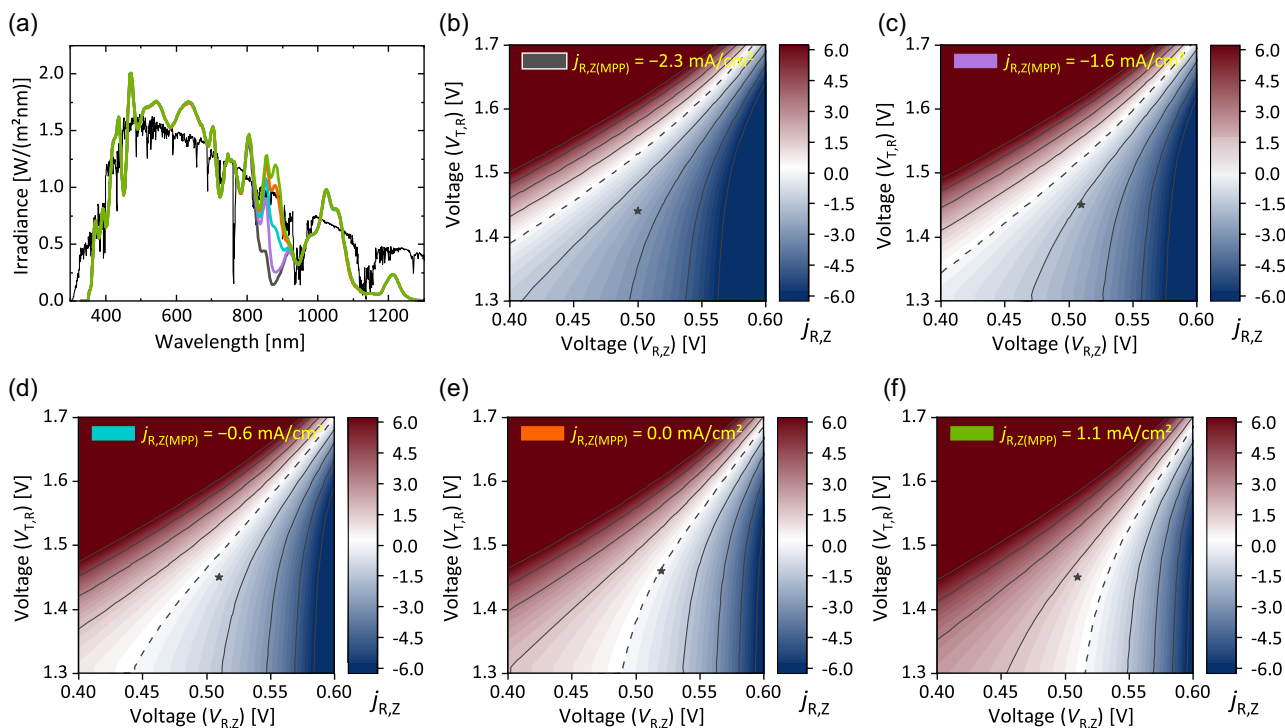
Figure 4. a) AM1.5g standard spectrum (black) and five solar simulator spectra created by adjusting the LED intensity in the wavelength regime between 800 and 900 nm (colored lines). b–d) Measured current density maps (red, white, and blue contour) and current density isolines (black) of a 3T TSC with p/n recombination junction where more current is photogenerated in the top cell than in the bottom cell. Additional current is injected into the bottom cell via terminal Z (blue contours). e) Same as (b–d) but for equal photocurrent generation in both subcells. At MPP, terminal Z remains largely idle (white color and dashed isoline), and the device behaves similar to a 2T TSC. f) Same as (b–d) but for higher photocurrent generation in the bottom cell. Surplus current is extracted through the additional terminal Z (red contours). Current maps are marked with a colored line indicating their corresponding spectrum in (a). The dashed isoline represents OPs where both subcells feature the same external current density. MPPs are marked with a black star in (b–f) The difference in external current at MPP, which is identical with the current extracted through/injected into the IBC subcircuit, is given in each figure.

This leads to an increased robustness against spectral variation as surplus current photogenerated in either subcell can be injected into or extracted through the additional terminal Z if necessary. In a 2T TSC, this additional photogenerated current would be lost to recombination, and the discrepancy would only be partially compensated by an increase in FF.[12]

2.3. Electrical Modeling

In this section, a model is devised to understand and describe the electrical behavior of 3T TSCs with p/n recombination junction. We use a similar simulation approach as in our previous publication where 3T TSCs with antiparallel junction have been investigated.[18] First, a case with equal photocurrent generation in both subcells is simulated. Individual subcells are modeled by fitting one-diode equations to j–V characteristics of single-junction perovskite and IBC SHJ cells fabricated at our institute[18,39] (further details are given in the Supporting Information). Electrical equivalent circuit simulations are conducted in LTspice[40] by using the equivalent circuit model depicted in **Figure 5**a with both subcircuits highlighted. Voltages across the IBC subcircuit, $V_{R,Z}$, are swept between 0 V ($j_{sc,IBC}$) and 0.7 V ($V_{oc,IBC}$) in 10 mV increments. For each of these bias steps, a j–V scan of the "2T" subcircuit is

performed, sweeping $V_{T,R}$ between 0 V ($j_{sc,perovskite}$) and 1.9 V ($V_{oc,perovskite} + V_{oc,IBC}$), also in 10 mV increments. The resulting array of curves is depicted in Figure 5b. For the sake of clarity, only every 100 mV step of $V_{R,Z}$ is depicted. As in the experiment, $V_{T,R}$ and $V_{R,Z}$ add up also in this simulation, shifting the "2T" subcircuit's V_{oc} point to higher voltages and thereby increasing PCE$_{T,R}$. Additionally, a good approximation of the perovskite top cell's j–V characteristics can be obtained by short circuiting the bottom cell's terminals by applying $V_{R,Z} = 0$ V, which yields the dashed black curve. The difference between real perovskite j–V characteristics and those obtained by this method, which are slightly affected by series resistance components of the bottom cell, is fairly marginal (see Figure S6, Supporting Information). The red-graded array of curves in Figure 5c shows the external current of the IBC subcircuit's terminals ($j_{R,Z}$) in response to different voltages ($V_{T,R}$) applied to the "2T" subcircuit. These are explicitly *not* the j–V characteristics of the IBC bottom cell. Extracting the IBC subcircuit's power output is explained for one OP given as a purple dot in Figure 5c. The innermost black and outermost red curves correspond to $V_{R,Z} = 0$ V and 0.7 V, respectively. All lines in between follow the same increments as described above with the exception that between 0.6 V and 0.7 V, every increment is shown to account for a fast change in IBC current density with small changes in voltage
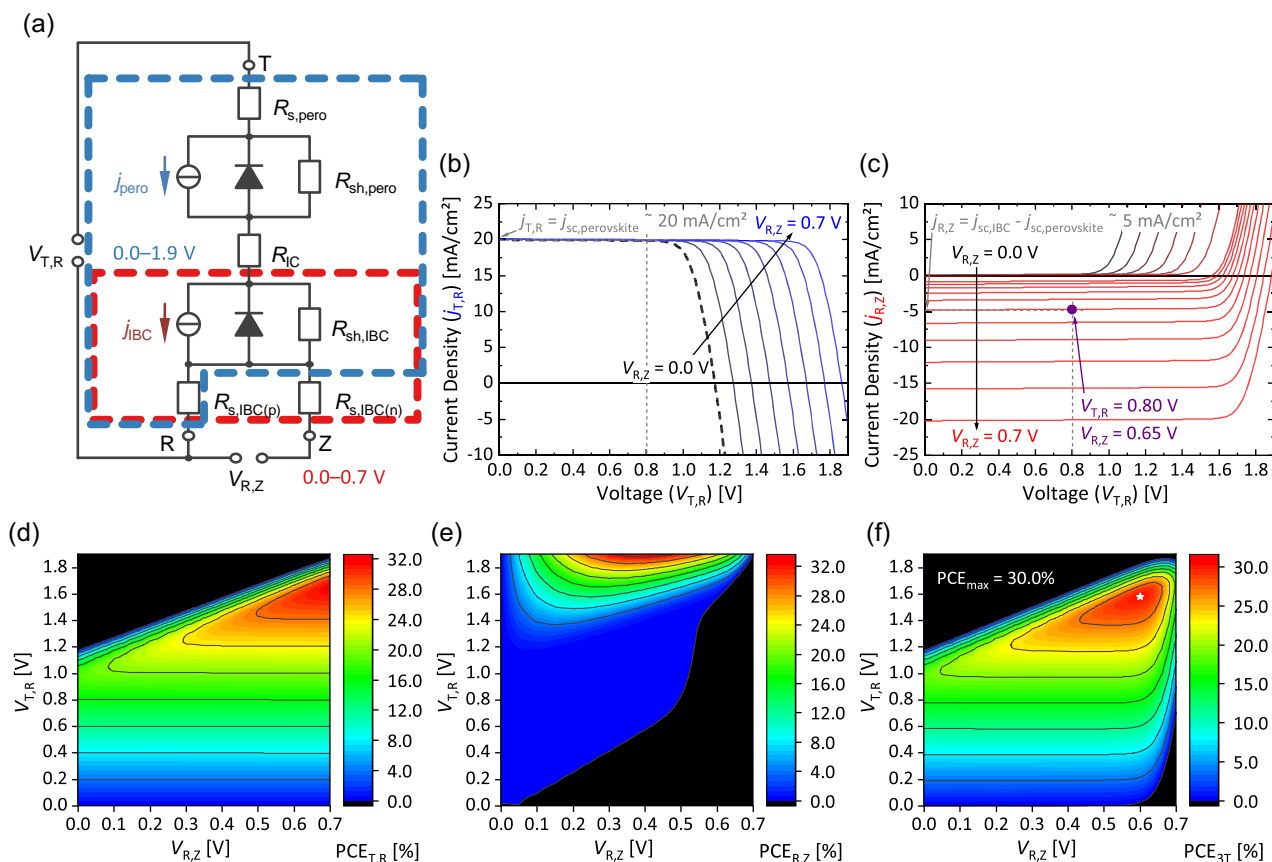
Figure 5. Electrical equivalent circuit used to describe the electrical behavior of a 3T TSC with p/n recombination junction. The "2T" and IBC subcircuit are highlighted in blue and red, respectively. The following abbreviations are used: perovskite top cell (pero); IBC bottom cell (IBC); series (R_s), shunt (R_{sh}), and interconnection (R_{IC}) resistance; current density (j). b) Simulated current density–voltage characteristics of the "2T" subcircuit for the investigated range of bias voltages ($V_{T,R}$ and $V_{R,Z}$). c) Simulated response of the IBC subcircuit to every $j_{T,R}$–$V_{T,R}$ sweep in (b). An example for extracting the power output for every bias condition is explained in the text for one operation point (purple dot). d) Simulated performance map showing the PCE of the "2T" subcircuit as a function of $V_{T,R}$ and $V_{R,Z}$. e) Same as (d) but for the PCE of the IBC subcircuit. f) Resulting simulated performance map of a 3T TSC with p/n recombination junction. A maximum PCE$_{3T}$ of 30% is achieved with improved subcells compared to the experimental results shown in Figure 3e (see Figure S5, Supporting Information, for further details). The device's MPP is marked with a white star. Note that the color scale in (d–f) is cut off at 0%.

(i.e., between $V_{MPP,IBC}$ and $V_{oc,IBC}$). In the selected example, the IBC cell is biased at $V_{T,R} = 800$ mV and $V_{R,Z} = 650$ mV. For this specific OP, a current density of approximately 5 mA cm^{-2} is injected into electrode Z (negative sign at the current density axis). This is because the here simulated IBC bottom cell would output roughly 15 mA cm^{-2} at 650 mV, whereas 20 mA cm^{-2} are extracted from the perovskite top cell at 800 mV. This causes an external current density difference of 5 mA cm^{-2}, which is compensated by injecting 5 mA cm^{-2} into the additional terminal. This is done for all pairs of $V_{R,Z}$–$j_{R,Z}$ for every $V_{T,R}$, and thus the power output (and thereby PCE) of the IBC subcircuit is calculated for every bias condition. In this way, the full j–V characteristics of a 3T TSC with p/n recombination junction can be obtained. The thus simulated arrays of curves agree well with measured data (Figure 3a,b). Since here, a 3T tandem with equal current generation in both subcells is simulated, electrode Z remains idle for most relevant OPs. In fact, the amount of photogenerated current mismatch and which subcell features a lower photocurrent can directly be observed from the way both arrays of curves are shifted

with respect to each other (more information given in Figure S7, Supporting Information).

Plotting the PCE of each subcell circuit versus $V_{T,R}$ and $V_{R,Z}$ gives the performance maps of the "2T" and the IBC subcircuit as well as for the entire device (as the summation of both) (Figure 5c–e). These simulated performance maps show a very good qualitative agreement with experimental results (Figure 3c–e). In contrast to those, an overall PCE$_{3T}$ of 30.0% is achieved here due to the simulation of improved subcells (see Supporting Information). For comparison, a 2T TSC is simulated using the same model but omitting the Z electrode. All other modeling parameters are kept the same. An identical PCE of 30.0% is achieved for a current-matched tandem, demonstrating the equivalency of performance in 2T and 3T TSCs in case of equal photogeneration in both subcells as discussed earlier. A key advantage of 3T over 2T TSCs is revealed when considering nonoptimal conditions. For the two device types, several photogeneration current-mismatch cases are investigated with a maximum of ± 5 mA cm^{-2} in either subcell while keeping a

constant combined j_{sc} of 40 mA cm^{-2} (**Figure 6**a). Such conditions are chosen to show the general electrical performance of 2T and 3T TSCs, not to simulate realistic illumination scenarios. In the current-matched scenario, both 2T and 3T TSCs feature equally high PCEs of 30%. A strong decrease in PCE is observed for 2T TSCs when the photogenerated current in one subcell is lower than in the other. This reduction in PCE is more severe if the perovskite top cell is limiting. This is due to a lower shunt resistance in the perovskite top than in the IBC SHJ bottom cell, which results in a lower overall FF.[41] In contrast, the PCE of 3T TSCs increases linearly if more current is generated in the top cell than in the bottom cell (here: 30.8% for +5 mA cm^{-2} in the top cell), whereas it slightly decreases for the opposite case (29.2%). It should be noted that under realistic spectral conditions, the combined photogeneration current density of both subcells also changes because of a reduction in illumination intensity.[42,43] Other than in the here used simplified electrical model, this would result in a saturation of PCE$_{3T}$ toward higher top cell photocurrents (positive mismatch) rather than an infinite linear increase as shown in Figure 6a. However, these simulations show that current matching is neither necessary nor the optimal operation point for 3T TSCs. Instead, maximizing photocurrent generation in the top cell is beneficial for the overall tandem performance. This is very similar to 4T TSCs[11] and has also been reported for other 3T TSCs as a defining feature of these devices.[16] It is also worth noting that despite the considerable variation in photogenerated current mismatch, there is no noticeable change in $V_{T,R,MPP}$ and $V_{R,Z,MPP}$ at maximum PCE for 3T TSCs (Figure 6b). Merely the external current distribution in the subcell circuits changes (as has been shown experimentally in Figure 4). This corroborates the results of the "spectral variation section" and is further interesting for implementing an MPP tracking routine for a 3T module. For 2T TSCs on the other hand, V_{MPP} changes more drastically with varying photocurrent-mismatch conditions.

When it comes to reliability, perovskite solar cells have yet to prove their viability in large-scale industrial applications. This is mainly because deposition techniques that ensure conformally covering a large area have yet to be developed.[41,44] On lab scale, perovskite films can be processed pinhole free with spin coating.[44] These processes, however, are not feasible in industrial-scale applications where the occurrence of pinholes remains a major concern.[41,45] The formation of pinholes leads to direct contact between the perovskites, ETL and HTL, and thereby a reduced shunt resistance. In Ref. [41] it was suggested that a high sheet resistance of the recombination TCO can mitigate local shunts stemming from pinholes. This, however, requires careful tuning of the fabrication process as it can affect the overall device efficiency. It might also be difficult to estimate the amount of expected pinholes in the perovskite layer (and thereby the necessary TCO sheet resistance) beforehand. Decreasing shunt resistance is further described as a major degradation mechanism for perovskite cells under negative voltage bias conditions as they can occur in a partially shaded module.[45–47]

Therefore, we investigate the robustness against shunting in the top cell for both 2T and 3T TSCs. We simulate the performance of both device types for a current-matched case and a total current density of 40 mA cm^{-2} while varying $R_{sh,perovskite}$ from 1 Ω cm^2 to 6 kΩ cm^2. All other modeling parameters are kept unchanged. The simulated j–V characteristics of all top cells and resulting 2T TSCs are depicted in Figure S9, Supporting Information for all investigated $R_{sh,perovskite}$ cases. The performance of both types of tandem devices only starts to deviate for $R_{sh,perovskite} < 1$ kΩ cm^2 (**Figure 7**a). Therefore, the range 1–6 kΩ cm^2 is not shown here. 3T TSCs appear to be slightly more robust against top cell shunting than 2T TSCs for all investigated cases. For 2T TSCs, the reduction in PCE is mainly driven by a steep decline in FF for more severe shunting (see Figure S9, Supporting Information). For $R_{sh,perovskite} \leq 10$ Ω cm^2, the FF rises again as the top cell is now almost completely shunted, and the j–V characteristics of the bottom cell are approached (see Figure S9, Supporting Information). For 3T TSCs, the reduction in PCE in the "2T" subcircuit ($j_{T,R}$–$V_{T,R}$) for very low $R_{sh,perovskite}$ can be partly compensated by redistribution of external current through terminal Z. In
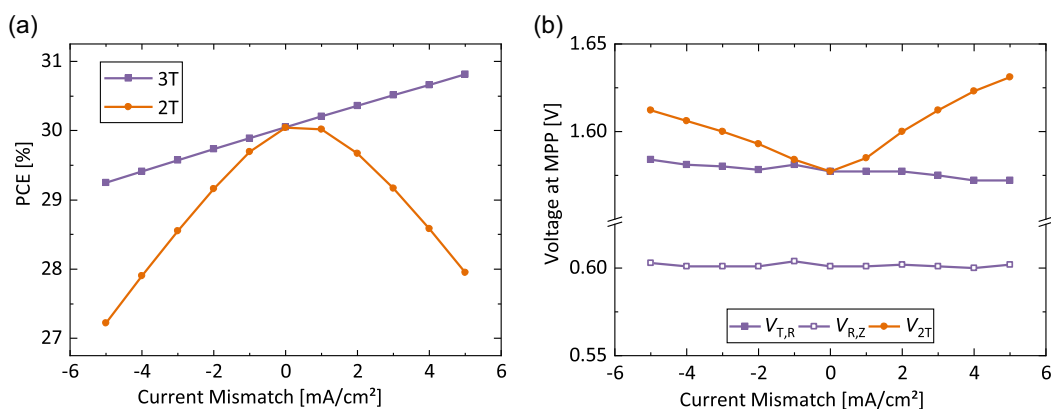

Figure 6. a) Simulated power conversion efficiencies of 2T (orange) and 3T TSCs (purple) under varying photocurrent-mismatch conditions. A positive (negative) mismatch indicates higher photocurrent generation in the top (bottom) cell. The total photogeneration current density is kept constant at 40 mA cm^{-2}. In the current-matched case, both device types feature an equally high PCE of 30%. b) Voltages at MPP of 2T (orange) and 3T TSCs (purple) under varying photocurrent-mismatch conditions. For 3T TSCs, both $V_{T,R}$ (closed symbols) and $V_{R,Z}$ (open symbols) are very stable for all investigated photocurrent-mismatch cases, whereas for 2T TSCs, V_{MPP} changes more drastically.
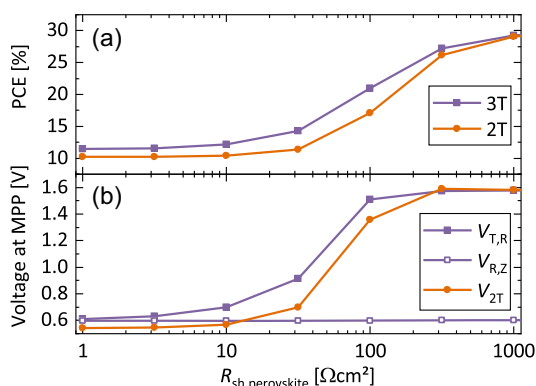
Figure 7. Simulated power conversion efficiencies of 2T (orange) and 3T TSCs (purple) for different perovskite top cell shunting cases. Both subcells are set to a j_{sc} of 20 mA cm^{-2}. The PCE loss in 2T TSCs is more severe than in 3T TSCs due to a reduction in FF and V_{MPP} with decreasing $R_{sh,perovskite}$. b) Voltages at MPP of 2T (orange) and 3T TSCs (purple) for different perovskite top cell shunt resistances. For 3T TSCs, $V_{R,Z}$ (open symbols) remains very stable, whereas $V_{T,R}$ (closed symbols) as well as V_{MPP} of 2T TSCs decrease drastically for more severe top cell shunting conditions.

case of a completely shunted top cell (1 Ω cm^2), the overall PCE$_{3T}$ is essentially that of an optically filtered IBC SHJ single-junction solar cell. Interestingly, $V_{R,Z}$ at MPP is completely unaffected by the top cell's condition (Figure 7b). In contrast, $V_{T,R}$ at MPP starts to decline rapidly for $R_{sh,perovskite} \leq 100$ Ω cm^2 due to a reduction of $V_{oc,perovskite}$ and $V_{MPP,perovskite}$. However, the reduction in V_{MPP} with decreased $R_{sh,perovskite}$ is even more severe for 2T TSCs.

3. Conclusions

In conclusion, we present an experimental realization of a 3T perovskite/silicon tandem solar cell with interdigitated rear contacts and p/n recombination junction between subcells. The electrical behavior of these devices cannot be described by a single j–V scan because both subcell circuits influence each other. Developing a suitable measurement procedure can therefore be challenging. 3T TSCs with p/n recombination junction as discussed in this article are optically and electrically very similar to 2T tandems with the additional terminal functioning as a current regulator. Unlike 2T tandems, however, current matching is not a prerequisite for proper operation. In fact, a maximum PCE is obtained when maximizing photocurrent generation in the top cell. In our case, a PCE of 24.9% has been achieved experimentally. It is further shown that the bias voltages at which the maximum PCE are achieved do not change appreciably with a variation in spectral conditions. This makes these devices robust against spectral variation and potentially simplifies establishing an MPP tracking algorithm. Lastly, an electrical equivalent circuit model is devised that describes well all experimentally observed characteristics of 3T TSCs with a p/n recombination junction. This model is then used to compare the robustness of 2T and 3T TSCs against photocurrent mismatch and perovskite top cell shunting. Moreover, it could be shown by using this simulation model that an overall PCE$_{3T}$ of 30% can already be achieved with moderately

improved subcells. For this, parameters of existing perovskite and IBC SHJ single-junction solar cells fabricated at HZB are used for subcell modeling in the simulations. Along with demonstrating pathways for potential optimization of 3T TSCs, the findings presented in this article will help researchers working on 3T TSCs to accurately measure the optoelectronic performance of these devices and interpret the obtained data.

4. Experimental Section

A schematic of the investigated device is shown in Figure 1. IBC silicon heterojunction (SHJ) bottom cells were fabricated on 250 μm thick 1–5 Ω cm phosphorous doped float-zone silicon (Si) wafers with (100) crystal orientation and 100 mm wafer diameter. Their rear side was textured with random pyramids while their front side was kept mechanically polished. All other Si layers—5 nm hydrogenated intrinsic amorphous silicon (a-Si:H(i), front and rear sides), 15 nm p-doped hydrogenated amorphous and n-doped hydrogenated nanocrystalline Si (a-Si:H(p)/nc-Si:H(n), rear side) as well as 100 nm hydrogenated nanocrystalline silicon oxide (nc-SiO$_x$:H, front side)—were deposited by plasma-enhanced chemical vapor deposition (PECVD) in an AKT1600 cluster tool operating at 13.56 MHz. Further information on the used PECVD layers and processes can be found in Ref. [48,49]. Rear contacts were formed by RF sputtering of 150 nm indium zinc oxide (IZO) and thermal evaporation of 1.5 μm silver (Ag). At the bottom cells' fronts, a 20 nm thick indium tin oxide (ITO) layer was RF sputtered. All IBC layers were patterned by photolithography. Before top cell fabrication, current density–voltage (j–V) characteristics were measured with a dual-source solar simulator under standard test conditions (STC) (Figure S1, Supporting Information). Afterwards, individual bottom cells with a designated illumination area of 1 cm^2 were cut out by a laser to inch-by-inch wafer pieces with the cell structure in the center. Further information on fabrication and characterization of IBC SHJ single-junction solar cells similar to those used in this study can be found in Ref. [39].

For the top cell absorber, a ≈550 nm-thick mixed cation, mixed halide perovskite layer in p–i–n configuration and with the molecular formula Cs$_{0.05}$(FA$_{0.83}$MA$_{0.17}$)$_{0.95}$Pb(I$_{0.83}$Br$_{0.17}$)$_3$ and a bandgap of 1.63 eV (following Ref. [50]) was applied by solution-based processes on top of a self-assembling monolayer (SAM).[7] The latter functions as a hole-transport layer (HTL) and was also applied by spin coating. At the front side, a 23 nm-thick C$_{60}$ electron-transport layer (ETL) was thermally evaporated, followed by a 20 nm tin oxide (SnO$_2$) buffer layer grown by atomic layer deposition (ALD). The top cells' front electrodes were then formed by RF sputtering of 100 nm IZO and a square Ag bus bar thermally evaporated through a shadow mask that defined the designated illumination area (1 cm^2) of these tandem devices. In a final step, lithium fluoride (LiF) was thermally evaporated as an antireflective coating. More details on the employed perovskite top cell fabrication process can be found in Ref. [12,51].

Following Ref. [19] the here investigated architecture is denominated perovskite/s/nuIBC (perovskite top cell connected in series with an n-type IBC bottom cell featuring one minority charge carrier contact). Its electrodes are labeled T, R, and Z (Figure 1); voltages across these electrodes are referred to as $V_{a,b}$ (with a and b being placeholders for T, R, and Z). A similar designation is used for current densities ($j_{a,b}$) and efficiencies (PCE$_{a,b}$). The overall PCE is denoted with the index "3T".

Current density–voltage characteristics of final 3T TSCs are measured under STC with a Wavelabs Sinus 70 class AAA LED solar simulator and a dual-channel source measure unit (SMU) interconnected as sketched in Figure S2a, Supporting Information. This way, a bias voltage can be applied to one subcircuit while simultaneously measuring the response of the other subcircuit, thereby scanning a variety of different operation points (OPs). If not stated otherwise, the term "OP" refers to all terminals being held at fixed voltages (e.g., the overall MPP). A more detailed description of the measurement procedure can be found in the Supporting Information or in literature.[28–30] For assessing the robustness

against spectral variation of these devices, the LED intensity of the solar simulator is adjusted in the spectral range between 800 and 900 nm to achieve either top or bottom cell limited operation (more details given later). To conduct electrical modeling, one-diode electrical equivalent circuit models are fit to j–V curves of real single-junction perovskite and IBC SHJ cells fabricated at our institute. The thus extracted diode characteristics and parasitic resistance values are then used in LTspice.[40]

Supporting Information

Supporting Information is available from the Wiley Online Library or from the author.

Conflict of Interest

The authors declare no conflict of interest.

Data Availability Statement

The data that support the findings of this study are available from the corresponding author upon reasonable request.

[1] W. Shockley, H. J. Queisser, *J. Appl. Phys.* **1961**, *32*, 510.
[2] T. Kirchartz, U. Rau, *Adv. Energy Mater.* **2018**, *8*, 1703385.
[3] National Renewable Energy Laboratory, https://www.nrel.gov/pv/cell-efficiency.html (accessed: August 2022).
[4] M. Kim, J. Jeong, H. Lu, T. K. Lee, F. T. Eickemeyer, Y. Liu, I. W. Choi, S. J. Choi, Y. Jo, H.-B. Kim, S.–I. Mo, Y.-K. Kim, H. Lee, N. G. An, S. Cho, W. R. Tress, S. M. Zakeeruddin, A. Hagfeldt, J. Y. Kim, M. Grätzel, D. S. Kim, *Science* **2022**, *375*, 302.
[5] M. Jošt, L. Kegelmann, L. Korte, S. Albrecht, *Adv. Energy Mater.* **2020**, *10*, 1904102.
[6] N. L. Chang, J. Zheng, Y. Wu, H. Shen, F. Qi, K. Catchpole, A. Ho-Baillie, R. J. Egan, *Prog. Photovoltaics Res. Appl.*, **2021**, *29*, 401.
[7] A. Al-Ashouri, E. Köhnen, B. Li, A. Magomedov, H. Hempel, P. Caprioglio, J. A. Márquez, A. B. Morales Vilches,

E. Kasparavicius, J. A. Smith, N. Phung, D. Menzel, M. Grischek, L. Kegelmann, D. Skroblin, C. Gollwitzer, T. Malinauskas, M. Jošt, G. Matič, B. Rech, R. Schlatmann, M. Topič, L. Korte, A. Abate, B. Stannowski, D. Neher, M. Stolterfoht, T. Unold, V. Getautis, S. Albrecht, *Science* **2020**, *370*, 1300.
[8] P. Tockhorn, J. Sutter, A. Cruz, P. Wagner, K. Jäger, D. Yoo, F. Lang, M. Grischek, B. Li, J. Li, O. Shargaieva, E. Unger, A. Al-Ashouri, E. Köhnen, M. Stolterfoht, D. Neher, R. Schlatmann, B. Rech, S. Albrecht, C. Becker, *Nat. Nanotechnol.* **2022**, *17*, 1214.
[9] Y. Yao, P. Hang, B. Li, Z. Hu, C. Kan, J. Xie, Y. Wang, Y. Zhang, D. Yang, X. Yu, *Small* **2022**, *18*, 2203319.
[10] CSEM/EPFL, https://www.csem.ch/page.aspx?pid=172296 (accessed: August 2022).
[11] T. Leijtens, K. A. Bush, R. Prasanna, M. D. McGehee, *Nat. Energy* **2018**, *3*, 828.
[12] E. Köhnen, M. Jošt, A. B. Morales-Vilches, P. Tockhorn, A. Al-Ashouri, B. Macco, L. Kegelmann, L. Korte, B. Rech, R. Schlatmann, B. Stannowski, S. Albrecht, *Sustainable Energy Fuels* **2019**, *3*, 1995.
[13] I. M. Peters, S. Sofia, J. Mailoa, T. Buonassisi, *RSC Adv.* **2016**, *6*, 66911.
[14] S. E. Sofia, N. Sahraei, J. P. Mailoa, T. Buonassisi, I. M. Peters, *IEEE J. Photovoltaics* **2017**, *7*, 934.
[15] S. Sakai, M. Umeno, *J. Appl. Phys.* **1980**, *51*, 5018.
[16] E. L. Warren, M. G. Deceglie, M. Rienäcker, R. Peibst, A. C. Tamboli, P. Stradins, *Sustainable Energy Fuels* **2018**, *2*, 1141.
[17] I. J. Park, J. H. Park, S. G. Ji, M.-A. Park, J. H. Jang, J. Y. Kim, *Joule* **2019**, *3*, 807.
[18] P. Tockhorn, P. Wagner, L. Kegelmann, J.-C. Stang, M. Mews, S. Albrecht, L. Korte, *Energy Mater.* **2020**, *3*, 1381.
[19] E. L. Warren, W. E. McMahon, M. Rienacker, K. T. VanSant, R. C. Whitehead, R. Peibst, A. C. Tamboli, *ACS Energy Lett.* **2020**, *5*, 1233.
[20] F. Gota, M. Langenhorst, R. Schmager, J. Lehr, U. W. Paetzold, *Joule* **2020**, *4*, 2387.
[21] J. P. Connolly, K. Ahanogbe, J.-P. Kleider, J. Alvarez, H. Kanda, M. Nazeeruddin, V. Mihailetchi, P. Baranek, M. Vogt, R. Santbergen, O. Isabella, in *37th European Photovoltaic Solar Energy Conf. and Exhibition (EU PVSEC 2020)*, EU PVSEC Committee, Lisbon, Portugal, September **2020**.
[22] Z. Djebbour, W. El-Huni, A. Migan Dubois, J.-P. Kleider, *Prog. Photovoltaics Res. Appl.* **2019**, *27*, 306.
[23] G. W. P. Adhyaksa, E. Johlin, E. C. Garnett, *Nano Lett.* **2017**, *17*, 5206.
[24] R. Santbergen, H. Uzu, K. Yamamoto, M. Zeman, *IEEE J. Photovoltaics* **2019**, *9*, 446.
[25] T. Nagashima, K. Okumura, K. Murata, Y. Kimura, in *Conf. Record of the Twenty-Eighth IEEE Photovoltaic Specialists Conf. (Cat. No. 0CH37036)*, IEEE, Anchorage, AK, USA, 15–22 September **2000**, pp. 1193–1196.
[26] J. M. Gee, *Solar Cells* **1988**, *24*, 147.
[27] M. Schnabel, M. Rienäcker, E. L. Warren, J. F. Geisz, R. Peibst, P. Stradins, A. C. Tamboli, *IEEE J. Photovoltaics* **2018**, *8*, 1584.
[28] M. Rienäcker, E. L. Warren, M. Schnabel, H. Schulte-Huxel, R. Niepelt, R. Brendel, P. Stradins, A. C. Tamboli, R. Peibst, *Prog. Photovoltaics Res. Appl.*, **2019**, *27* 410.
[29] M. Schnabel, H. Schulte-Huxel, M. Rienäcker, E. L. Warren, P. F. Ndione, B. Nemeth, T. R. Klein, M. F. A. M. van Hest, J. F. Geisz, R. Peibst, P. Stradins, A. C. Tamboli, *Sustainable Energy Fuels* **2020**, *4*, 549.
[30] J. F. Geisz, J. Buencuerpo, W. E. McMahon, T. R. Klein, A. C. Tamboli, E. L. Warren, in *48th IEEE Photovoltaic Specialists Conf. (PVSC)*, IEEE, Fort Lauderdale, FL, USA, 20–25 June **2021**, pp. 0154–0157.
[31] H. Liu, C. D. Rodríguez-Gallegos, Z. Liu, T. Buonassisi, T. Reindl, I. M. Peters, *Cell Rep. Phys. Sci.* **2020**, *1*, 100037.

[32] K. T. VanSant, E. L. Warren, J. F. Geisz, T. R. Klein, S. Johnston, W. E. McMahon, H. Schulte-Huxel, M. Rienäcker, R. Peibst, A. C. Tamboli, *iScience* **2022**, *25*, 104950.

[33] J. H. Park, S. G. Ji, I. J. Park, S. K. Hwang, H. W. Lim, J. Y. Kim, *Cell Rep. Phys. Sci.* **2022**, *3*, 101076.

[34] T. Tayagaki, K. Makita, T. Tachibana, H. Mizuno, R. Oshima, H. Takato, T. Sugaya, *Sol. Energy Mater. Sol. Cells* **2021**, *221*, 110901.

[35] L. L. Senaud, B. Kamino, J. Geissbühler, G. Christmann, F. Sahli, P. Wyss, D. L. Bätzner, D. Lachenal, Q. Jeangros, C. Ballif, B. Paviet-Salomon, C. Allebé, M. Kikelj, *presented at the 8th World Conf. on Photovoltaic Energy Conversion (WCPEC–8)*, Milan, Italy, 26–30 September **2022**.

[36] H. Schulte-Huxel, D. J. Friedman, A. C. Tamboli, *IEEE J. Photovoltaics* **2018**, *8*, 1370.

[37] H. Schulte-Huxel, R. Wittek, S. Blankemeyer, M. Köntges, *Prog. Photovoltaics Res. Appl.* **2022**, https://doi.org/10.1002/pip.3643.

[38] W. E. McMahon, H. Schulte-Huxel, J. Buencuerpo, J. F. Geisz, M. S. Young, T. R. Klein, A. C. Tamboli, E. L. Warren, *IEEE J. Photovoltaics* **2021**, *11*, 1078.

[39] P. Wagner, A. Cruz, J.-C. Stang, L. Korte, *IEEE J. Photovoltaics* **2021**, *11*, 914.

[40] Analog Devices, https://www.analog.com/en/design-center/design-tools-and-calculators/ltspice-simulator.html (accessed: August 2022).

[41] C. Blaga, G. Christmann, M. Boccard, C. Ballif, S. Nicolay, B. A. Kamino, *Sustainable Energy Fuels* **2021**, *5*, 2036.

[42] M. Jošt, E. Köhnen, A. B. Morales-Vilches, B. Lipovšek, K. Jäger, B. Macco, A. Al-Ashouri, J. Krč, L. Korte, B. Rech, R. Schlattmann, M. Topič, B. Stannowski, S. Albrecht, *Energy Environ. Sci.* **2018**, *11*, 3511.

[43] M. T. Hörantner, H. J. Snaith, *Energy Environ. Sci.* **2017**, *10*, 1983.

[44] P. Kaienburg, P. Hartnagel, B. E. Pieters, J. Yu, D. Grabowski, Z. Liu, J. Haddad, U. Rau, T. Kirchartz, *J. Phys. Chem. C* **2018**, *122*, 27263.

[45] K. Brecl, M. Jošt, M. Bokalič, J. Ekar, J. Kovač, M. Topič, *Sol. RRL* **2022**, *6*, 2100815.

[46] C. C. Boyd, R. Cheacharoen, T. Leijtens, M. D. McGehee, *Chem. Rev.* **2018**, *119*, 3418.

[47] L. Xu, J. Liu, W. Luo, N. Wehbe, A. Seitkhan, M. Babics, J. Kang, M. De Bastiani, E. Aydin, T. G. Allen, M. Alamer, W. Yan, F. Xu, A. U. Rehman, S. De Wolf, *Cell Rep. Phys. Sci.* **2022**, *3*, 101026.

[48] A. B. Morales-Vilches, E.-C. Wang, T. Henschel, M. Kubicki, A. Cruz, S. Janke, L. Korte, R. Schlatmann, B. Stannowski, *Phys. Status Solidi A* **2020**, *217*, 1900518.

[49] L. Mazzarella, Y.-H. Lin, S. Kirner, A. B. Morales-Vilches, L. Korte, S. Albrecht, E. Crossland, B. Stannowski, C. Case, H. J. Snaith, R. Schlatmann, *Adv. Energy Mater.* **2019**, *9*, 1803241.

[50] M. Saliba, T. Matsui, J.-Y. Seo, K. Domanski, J.-P. Correa-Baena, M. K. Nazeeruddin, S. M. Zakeeruddin, W. Tress, A. Abate, A. Hagfeldt, M. Grätzel, *Energy Environ. Sci.* **2016**, *9*, 1989.

[51] E. Köhnen, P. Wagner, F. Lang, A. Cruz, B. Li, M. Roß, M. Jošt, A. B. Morales-Vilches, M. Topič, M. Stolterfoht, D. Neher, L. Korte, B. Rech, R. Schlatmann, B. Stannowski, S. Albrecht, *Sol. RRL* **2021**, *5*, 2100244.